UNIVERSITÀ POLITECNICA DELLE MARCHE
Repository ISTITUZIONALE

Modelling the creep behavior of an AlSi10Mg alloy produced by additive manufacturing

This is the peer reviewd version of the followng article:

Original
Modelling the creep behavior of an AlSi10Mg alloy produced by additive manufacturing / Paoletti, C.; Santecchia, E.; Cabibbo, M.; Cerri, E.; Spigarelli, S.. - In: MATERIALS SCIENCE AND ENGINEERING A-STRUCTURAL MATERIALS PROPERTIES MICROSTRUCTURE AND PROCESSING. - ISSN 0921-5093. - 799:(2021). [10.1016/j.msea.2020.140138]

Availability:
This version is available at: 11566/286694 since: 2024-03-20T16:17:14Z

Publisher:

Published
DOI:10.1016/j.msea.2020.140138

Terms of use:

The terms and conditions for the reuse of this version of the manuscript are specified in the publishing policy. The use of copyrighted works requires the consent of the rights' holder (author or publisher). Works made available under a Creative Commons license or a Publisher's custom-made license can be used according to the terms and conditions contained therein. See editor's website for further information and terms and conditions.
This item was downloaded from IRIS Università Politecnica delle Marche (https://iris.univpm.it). When citing, please refer to the published version.

note finali coverpage

(Article begins on next page)

24 July 2024

POST PRINT (ACCEPTED COPY)

Modelling the creep behavior of an AlSi10Mg alloy produced by additive manufacturing

C.Paoletti[1*], E. Santecchia[1], M.Cabibbo[1] , E.Cerri[2], S.Spigarelli[1]

1. DIISM Università Politecnica delle Marche, via Brecce Bianche 60131 Ancona (Italy)

2. DIA Università di Parma, V.le G. Usberti 181/A, 43124 - Parma (Italy)

https://doi.org/10.1016/j.msea.2020.140138

Received 25 June 2020; Received in revised form 19 August 2020; Accepted 19 August 2020

Available online 28 September 2020

0921-5093/© 2020 Elsevier B.V. All rights reserved.

Modelling the creep behavior of an AlSi10Mg alloy produced by additive manufacturing

C.Paoletti[1*], E. Santecchia[1], M.Cabibbo[1] , E.Cerri[2], S.Spigarelli[1]

1. DIISM Università Politecnica delle Marche, via Brecce Bianche 60131 Ancona (Italy)

2. DIA Università di Parma, V.le G. Usberti 181/A, 43124 - Parma (Italy)

Abstract

AlSiMg alloys produced by additive manufacturing possess an extremely fine and complex microstructure that in many ways defies the most widely used phenomenological models, which, in fact, have turned out to be poorly suited for predicting their mechanical properties. The underlying rationale for the peculiar properties of these alloys has been qualitatively established, however the need for a constitutive model with better predictive capability is still strong. To this aim, the ultra-fine microstructure was described by using a model-material (MM) consisting of soft and hard zones deforming under a similar strain rate. A physically-based set of constitutive equations which took into account also the coarsening/ripening phenomena of the Si-particles was used to predict the creep behavior of the MM. In parallel, the creep response of an AlSi10Mg alloy produced by additive manufaturing and tested in the as-deposited condition was investigated at temperatures ranging from 150 to 225°C. The minimum creep rate curves obtained for the MM by the constitutive model were then compared with the experimental data obtained by testing the real alloy under constant load in different initial states. The excellent correlation between model curves and experimental results was discussed, taking into account the evolution of the microstructure during creep.

* corresponding author
email: c.paoletti@pm.univpm.it

1. Introduction

Among the additive manufacturing (AM) techniques applied to metals and alloys, laser powder bed fusion (LPBF) is now taking the lead [1–3]. During LPBF, the laser beam selectively fuses regions of a powder bed and builds up new parts layer-upon-layer using a computer aided design (CAD) model. The quick action of the laser gives rise to very high cooling rates (~10^6 °C/s) and the reiterated fusion process on the upper layers acts as a thermal treatment on the lower and already solidified layers, generating unique microstructures and peculiar mechanical properties [4,5]. The extensive investigations carried out on the macrostructure, microstructure and mechanical properties of AlSi10Mg processed by AM have clearly outlined several important features that can be summarized as follows:

i. the mesostructure, i.e. the combination of structural features at intermediate scale (5-100μm), in the as-deposited material is usually formed by columnar Al grains with a diameter of several microns. On a finer sub-micron scale, these grains are formed by smaller long cells with a diameter of a few hundreds of nm separated by Si- Mg-rich eutectic regions. These long cells, in turn, are fragmented in more equiaxed sub-cells, again with a diameter of a few hundreds of nm (500 in [6]), separated by a network of Si-rich eutectic regions;

ii. the Si-rich eutectic regions are usually decorated with a fine dispersion of nanometric Si particles. Yet, one can find as-built alloys in which the eutectic region contains a well-defined semi-continuous chain of Si of Si particles in the Si-Mg-rich areas, as in [7,8], and materials that develop this structure only after an annealing treatment [9,10], since the initial and continuous network is formed by much finer (a few nm) particles and/or by coarser particles that spheroidize upon heating. These differences can be safely attributed to the different processing parameters, although it has been clearly

demonstrated that the number of particles in the as-deposited state depends on sample size [10];

iii. also the cell interiors contain widely dispersed Si-particles;

iv. the extreme fineness of the microstructure results in very high mechanical properties of the as-deposited samples at the expense of a low ductility. Typical UTS values for as-built samples range from 340 [11] to 473 MPa [12], the lower values being usually observed when the strain to fracture is particularly low (1.5% and 7.7% in [11] and [12] respectively);

v. the excessive brittleness is somewhat reduced by an annealing or stress-relieving treatment, which causes an increase in strain to fracture but substantially reduces the UTS [7,9,13]. A stress-relieving treatment carried out at 300°C causes the partial separation of the continuous Si network which outlines the cells as well as a moderate coarsening of the Si particles.

The Al–Si–Mg alloys are potentially good candidates for many applications, such as motor racing, automotive and aerospace industries, as well as for the production of heat exchanger parts. These materials, and the AlSi10Mg alloy among them, are thus widely used for lightweight and thin walled casting parts. In this rapidly developing context, it is only natural that most of the studies have investigated the correlations between the structure, heat treatments and room temperature mechanical properties of the AM-produced AlSi10Mg, while only a minority of them have considered the high-temperature properties of this material. Aluminum alloys have been traditionally known to exhibit poor creep resistance, and a result the study of creep of die-cast alloys has been frequently neglected. Creep of AM AlSi10Mg alloy, was thus investigated only by Read et al. [11], who merely carried out 3 experiments, and by Elan Uzan et al [14]. The latter investigated the creep response of the alloy after stress-relieving at 300°C for 2 h by carrying out 7 experiments (4 tests at 225°C under 117, 127, 137 and 147 MPa, and 3 additional tests under 117MPa at 250, 275 and 300°C). Their data, however, provide a detailed

picture of the material response at a temperature that is well above any operational limit for an alloy like AlSi10Mg, and thus, although very useful to interpret its properties, are of limited interest for any potential application of this alloy.

An interesting point is that there is ample evidence that at high temperature, during annealing [7,8] or creep [14], Si particles spheroidize and undergo ripening. Thus, at the end of the test, the eutectic region assumes the form of a densely spaced distribution of fine Si globular particles. On the other hand, the lack of further experimental results on the creep response needs to be addressed, since it has been clearly demonstrated that AlSi alloys behave as metal-matrix composites of some sort in which Si particles act as reinforcements [15,16]. In this sense, the creep response of these natural composites reinforced with nm-sized Si particles is an intriguing subject that deserves a detailed investigation. The aim of this study was threefold: 1. to provide a physically-based constitutive model for the description of the creep results, created on the bases of the already existing evidences about the microstructure and its evolution of AlSi10Mg produced by AM; 2. to fill the gap in the knowledge of high temperature response by investigating the creep behavior of alloy produced by AM in a temperature range quite close to any potential application; 3. to validate the prediction of the physical model with the new matrix of experimental creep data.

2. Material model and constitutive equations

2.1 Material model

The first aim of this study was to provide a model-material (MM) in which all the major features of the microstructure of AM alloys can be easily recognized. The basic assumption is that the creep response, in its essence, and in particular the minimum creep rate dependence on stress and temperature, substantially depends on the microstructural features, that is, on dislocation movement and dislocation-obstacle interactions. The structural features at a macro- and meso- scales (size of

the melt pools, size and morphology of the columnar grains, inhomogeneous distribution of solute elements etc) are here thought to have an effect only on the damage mechanisms and thus cause early onset of tertiary creep.

The previous section provides a clear description of the typical sub-micron microstructural features of the as-deposited alloy, which consists of very small cells surrounded by a network of eutectic regions that, after deposition, annealing or at the very beginning of the test, appear to be decorated with a fine and dense distribution of nm-sized Si particles. The cells, which contain remote fine particles, clearly consitute a soft zone dislocation can easily pass through. By contrast, the eutectic regions form hard zones which represent a strong obstacle to dislocation motion [6]. On these bases, the simple rule of mixtures was used to create a model-material which exemplifies the microstructure of a typical AlSi10Mg alloy produced by AM (Figure 1). The MM is thus thought as a simplified depiction of the real microstructure, described at a sub-micron scale, while the macro- and mesostructural features are not considered. The MM here designed is formed by cells with a diameter of 500 nm surrounded by a network of hard zones in which a fine distribution of Si-particles of size 50 nm is dispersed. Once the dislocation arrives at the boundary of the hard zone, it encounters successive lines of particles whose center-to-center distance is assumed to be 100 nm, which gives a surface-to-surface distance of 50 nm. Particles in cell interiors are assumed to be homogeneously distributed, the initial spacing (center-to-center distance) between them being 200 nm. The total volume fraction of the hard zones in the eutectic regions is taken as 25%, the rest being the softer cell interiors. A certain amount of Si and Mg in both the soft and hard zones are in solid solution. Particles coarsen during creep and, as a result, the interparticle distance becomes larger. For a constant volume fraction of the reinforcing phase, the interparticle spacing can be considered to be proportional to the particle diameter, giving

$$\mathrm{L} = \mathrm{L}_0 \frac{d}{d_0} \qquad (1)$$

where L and L_0 are the surface to surface particle distance, d and d_0 the particle size at time t and at the beginning of the test, respectively. With regards to the particles inside the cells, it was assumed

that the particle distance actually increased with time due to ripening up to half of the cell diameter (250 nm) and remained constant for a longer duration. This assumption implies that, even for long times of exposure, at least one single particle remains in the cell interior. Figure 1, which schematically illustrates the evolution of the MM microstructure during high-temperature exposure, clearly suggests that, in the presence of coarsening/ripening phenomena, the material becomes more and more homogeneous in terms of particle distribution.

The other main basic assumption necessary to develop a physical-based model that is easy to handle is that both the hard and soft zones deform with a similar strain rate. In such a case, the total stress can be calculated as

$$\sigma = f_H\, \sigma_H + (1 - f_H)\sigma_S \qquad (2)$$

where σ_H and σ_S are the stresses acting on the hard and soft zones, respectively [17].

It is worth noting that the analysis in the following will not take into account any possible effect of the prior residual stresses introduced in the creep samples by the heat-gradients typical of AM. The reason is quite straightforward, since it can be considered that, during sample heating and holding at high T (the whole process lasted 3 h), high-temperature exposure should be enough to cause the progressive reduction of any residual stress.

2.2 Equations for Dislocation Creep in Al: Strengthening Terms

The constitutive model here used was developed for Cu by Sandström [18–20] and later implemented to describe high-temperature deformation of aluminum alloys of increasing microstructural complexity [21–24]. The model represents an excellent alternative to more traditional approaches based on phenomenological power-law relationships, since it is based on equations describing the physics of phenomena. The model is articulated on the following equations (the meaning of the symbols is given in Table 1, while the full derivation of the model can be found in the above-mentioned references and is summarized in Appendix A):

$$\sigma = \sigma_0 + \sigma_p = \sigma_0 + \alpha m G b \sqrt{\rho} \qquad (3)$$

$$\dot{\varepsilon}_m = \frac{2M_{cg}\tau_l bL}{m}\left(\frac{\sigma_\rho}{\alpha mGb}\right)^4 \quad (4)$$

$$M_{cg} \cong \frac{D_{0L}b}{kT} exp\left(\frac{\sigma_\rho b^3}{kT}\right) exp\left\{-\frac{Q_L}{RT}\left[1-\left(\frac{\sigma_\rho}{R_{max}}\right)^2\right]\right\} exp\left(-\frac{U_{ss}}{RT}\right) \quad (5)$$

$$R_{max} = 1.5(R^a_{UTS} + \sigma_{Or})\frac{G_T}{G_{RT}} \quad (6)$$

The stress σ_0 represents the strengthening contribution due to the interaction between fine particles and dislocations. Under high applied stress and/or at low temperature, the particle-strengthening effect is equal to the Orowan stress (σ_{Or}), here calculated by the well-known simple formula [25]:

$$\sigma_{Or} = \frac{084mGb}{L} \quad (7)$$

Under low stresses, when Orowan by-pass cannot occur, and at high temperatures, dislocations can still overcome particles by different thermally activated mechanisms. In this study, the maximum temperature was 225°C and the stresses in many cases were close or even above the yielding of the material. On these bases, similarly to nanoparticle-strengthened composites, where $\sigma_0 \approx \sigma_{Or}$ [23] for temperatures below 250°C, the particle strengthening term was here assumed to be equal to the Orowan stress. For the sake of simplicity, it is convenient to mention that, in the evaluation of the material strength, Equation (3) does not take into account the stress required to move the dislocation in the absence of other dislocations nor the viscous drag stress due to solute atoms, since both these quantities are usually much lower than the particle strengthening term (see [21,22] for a detailed discussion).

2.3 Evolution of particle strengthening term during high-temperature exposure

Once they precipitate to the equilibrium volume fraction, particles evolve during subsequent high-temperature exposure by a process whose kinetics is frequently described by the Ostwald ripening equation in the form

$$d^3 = d_0^3 + \frac{64\gamma C_\infty V_m^2}{9RT} D_{eff} t \quad (8)$$

where d_0 is the initial particle size, d the particle size at time t, γ the interfacial energy, C_∞ the equilibrium concentration of the species that form the particles, V_m the molar volume of the particle. D_{eff} is the effective diffusion coefficient that, following Taneike et al [27], can be written as

$$D_{eff} = D_{Ls} + A_{p1}\rho D_{ps} + A_{p2}\rho_m D_{ps} \quad (9)$$

where $D_{Ls}=D_{0Ls}\exp(-Q_{Ls}/RT)$ is the lattice diffusion coefficient of the element forming the particle, $D_{ps}=D_{0ps}\exp(-Q_{ps}/RT)$ the corresponding pipe-diffusion coefficient and ρ_m the mobile dislocation density. A_{p1} is the effective sectional area for pipe diffusion along dislocations, while A_{p2} is a much wider effective sectional area for diffusion which takes into account the scavenging effect of solute atoms by moving dislocations.

The second term on the right-hand side of Equation (9) represents the effect of pipe diffusion along dislocation cores. Although it takes into account the whole dislocation population, its magnitude becomes significant only for very high stresses and/or low temperatures. This statement can be easily confirmed by a rough calculation based on the expression for the lattice diffusivity of the most significant particle constituent of the material investigated, i.e. Si. For the diffusion of Si in Al, Q_{Ls} =124 kJ mol^{-1} [28]. By taking Q_{ps}=0.6 Q_{Ls}, the diffusion measurements by Legros et al. [29] give D_{0Ls} = 2.7x10^{-5} and D_{0ps} = 2.6x10^{-6} m^{2}s^{-1}. With $A_{p1}=10b^2$ [30], the second term on the right-hand side of Equation (9) becomes comparable with D_{Ls} only at temperatures below 175°C with ρ_m =10^{13} m^{-2}. In other terms, pipe diffusion along dislocation core becomes significant for highly stressed samples only when the temperature is so low that Ostwald ripening is slow and has negligible effects.

The last term on the right-hand size of Equation (9) represents the effect of the scavenging mechanism: traveling dislocations are thought to collect and drag solute atoms from the matrix, thus assisting the solute transport mechanism. The effective sectional area A_{p2} is thus by far wider than A_{p1} and could be in principle considered a function of dislocation velocity, since, for a given duration, the scavenging effect becomes more effective when dislocation velocity increases [27]. On these bases, Equation (9) becomes

$$D_{eff} \approx D_{Ls} + A_{p2}\rho_m D_{ps} \quad (10)$$

Based on the Orowan equation

$$\dot{\varepsilon} = \frac{b}{m}\rho_m v_m \quad (11)$$

where v_m is the dislocation velocity. Combined with Equation (10), Equation (11) gives

$$D_{eff} = D_{Ls} + \frac{A_{p2}m}{bv_m}\dot{\varepsilon}D_{ps} \quad (12)$$

If A_{p2} is indeed supposed to be proportional to the dislocation velocity v_m, then

$$D_{eff} = D_{Ls}\left(1 + B'\dot{\varepsilon}\frac{D_{ps}}{D_{Ls}}\right) = D_{Ls}\left[1 + B\dot{\varepsilon}exp\left(\frac{Q_{Ls}-Q_{ps}}{RT}\right)\right] \quad (13)$$

which is formally analogous to a similar equation proposed by Cohen [31]. In this expression, the B parameter ($B=B'D_{ps0}/D_{pL0}$) does not depend on stress, strain rate nor temperature, as in the case of the Cohen equation. The Ostwald ripening equation thus becomes

$$d^3 = d_0^3 + K_g D_{Ls}t + K_g D_{Ls}Bexp\left(\frac{Q_{Ls}-Q_{ps}}{RT}\right)\dot{\varepsilon}t \quad (14)$$

with

$$K_g = \frac{64\gamma C_\infty V_m^2}{9RT} \quad (15)$$

This expression is almost equivalent to that used in [27], and contains a term which increases linearly with $\dot{\varepsilon}t$, that is, with strain. Thus, one can state that the acceleration of particle coarsening in strained samples depends on strain rate [27,31], stress (since strain rate is a function of applied stress) [32,33] or strain [30,34,35], with each of these assertion being justified by Equation (14). By taking again Q_{Ls} =124 kJ mol^{-1} (with Q_{ps}=0.6 D_{0Ls}), the two remaining parameters to be estimated are $D_{pL0}K_g$ and B. To simplify the calculation, the weak dependence of K_g on temperature can be neglected. The data on the ripening of Si particles after 6 h at temperatures between 300 and 400°C in an Al-12Si alloy produced by AM [13] can then be used to estimate $D_{0Ls}K_g$ even at this early stage of the analysis, giving 2x10^{17} nm^3 h^{-1}(Figure 2).

3. Experimental technique

Dog-bone creep samples in an Al-9.6%Si-0.38%Mg alloy with a gauge length of 25 mm and a square section of 3 mm x 3mm were built using an SML500 machine with the following deposition parameters: substrate temperature 150°C, laser power 350 W, spot size 80 μm, scan speed 1.15 m/s, hatch spacing 170 μm, layer thickness 50 μm. The growth direction was parallel to the sample axis (loading direction).

Constant load tensile creep experiments were carried out in air on the as-deposited samples at 150, 175, 205 and 225°C. The samples were mostly strained up to rupture, although, in some cases, the tests were interrupted at the early onset of the tertiary region. The samples were heated in a three-zone furnace, and both the elongation, measured by ±20 mm full scale displacement LVDT, and temperature were continuosly recorded during the test. Temperature was measured by 4 thermocouples, to ensure that deviation from set value did not exceed 1°C.

The degradation of the mechanical properties due to high-temperature exposure was quantified by Vickers Hardness measurements along the gauge length and on the samples' heads.

Surfaces for the FEGSEM inspections were grounded and polished mechanically and then etched using Keller's reagent at room temperature for few seconds. Microstructure inspections were carried out by scanning electron microscopy using a Zeiss^{TM} ULTRA-55$^{®}$ field emission scanning electron microscope (FEGSEM). Element point analyses were obtained by using energy dispersive X-ray spectroscopy (EDS), operated at an acceleration voltage of 20 kV, a beam at spot size within 2 μm and using a working distance of 16 mm.

4. Experimental results

4.1 Microstructure of the as-deposited samples

Figure 3 shows a representative example of the microstructure of the as-deposited alloy creep tested in the present study. Figure 4 shows the microstructure at higher magnification, and EDS point analyses in a Si-rich region of dark-grey rounded particles (red spot in the Figure) and in the Al-

matrix (blue spot in the Figure). Since the EDS actually measured the composition in a region larger than the spots in Figure 4, in both cases the analysis included a portion of the matrix and a number of particles. Yet, even this simple analysis confirms that the eutectic regions ar much richer in Si, as attested by the presence of a higher number of particles.

As expected, the microstructure presents all the typical features of materials processed by AM, which are clearly delineated in [6]. Thus, at a finer scale, the microstructure is mainly formed by cells of a few hundreds nm in size surrounded by eutectic regions.

A major difference between the material investigated in this study and the alloy of similar composition described in [6] is given by the size of the Si particles. The alloy studied by Wu et al was characterized by particles of extremely fine size, while the alloy investigated in the present study is more similar to the materials investigated in [10], since the Si particles are larger.

4.2 Mechanical testing results

Figure 5-6 show a representative creep curves. The shape of the curve is fully conventional, with a well defined primary region, a minimum creep rate range, and a tertiary stage which rapidly leads to fracture (Figure 6). As it usually happens when the alloy tested is in the as-deposited state, the fracture elongation is limited, rarely exceeding ε=0.06.

Figure 7 plots the minimum creep rate ($\dot{\varepsilon}_m$) as a function of the stress at the beginning of the test (for samples tested above the yield stress, in the estimation of the real stress at the beginning of the test, the instantaneous plastic elongation and the consequent reduction in area were considered). The figure plots the straight lines that represent the conventional phenomenological power-law equation

$$\dot{\varepsilon}_m = A(T)\sigma^n \qquad (16)$$

where $A(T)$ is a temperature dependent parameter, and the stress exponent n increases with temperature decreasing from 15 to 22. These very high values of the stress exponent are indeed typical of these alloys, and are usually attributed to the strengthening effect of particle-dislocation interaction acting at sub-micron scale [15]. A considerable scatter is observed in the case of the

most numerous dataset, the one obtained at the lower temperature. This scatter can be attributed to the heterogeneities of the mesostructure typical of AM-samples, which could accelerate damage mechanisms leading to early fracture. For this reason, only the lower-bound values of the creep rate were used in the following.

Figure 8 shows the variation of the hardness with the time of exposure at high temperatures (150 and 205°C) measured on the samples' heads and along the gauge length. As it can be reasonably expected, both on the heads and the gauge length, the hardness decreases with increasing exposure time. Yet, the hardness in the gauge length remains invariably much lower than that on the heads, notwithstanding the stress introduced a high dislocation density in the sample, in particular in the highly-loaded specimen (short test duration). This behavior is indeed typical of many materials in which the presence of an applied stress at high temperature, and the consequent straining, causes an accelerated degradation of the microstructure, and, in particular, an enhanced particle ripening and/or coarsening [27,30,32–35]. Thus, Figure 8 represents an unambiguous indication that the material under study underwent a stress- (or strain-) accelerated microstructural degradation during creep.

5. Discussion

5.1 Creep of as-deposited alloy

The set of constitutive equations illustrated in Section 3 provides a tool for predicting the MM behavior which, in the first place, is thought to well approximate the real AM alloy, once the coarsening/ripening law of the strengthening particles is properly assessed. At the time corresponding to the minimum creep rate, Equation (14) can be tentatively rewritten in the form

$$d^3 = d_0^3 + K_g D_{pL0} t_m exp\left(\frac{Q_{Ls}}{RT}\right)\left[1 + exp\left(\frac{Q_{Ls}-Q_{ps}}{RT}\right) B\dot{\varepsilon}_{av}\right] \quad (17)$$

where $\dot{\varepsilon}_{av}$ is the average creep rate experienced by the sample until the minimum value is reached (the time t_m as obvious does not include heating and holding time before loading, in the assumption that this durations are too short to cause an important increase in particle size). In the case of the

curve illustrated in Figure 5, it results that $\dot{\varepsilon}_{av} \cong 10\dot{\varepsilon}_m$, which was used for all the experiments, giving

$$d^3 = d_0^3 + K_g D_{pL0} t_m exp\left(\frac{Q_{Ls}}{RT}\right)\left[1 + 10\ exp\left(\frac{Q_{Ls}-Q_{ps}}{RT}\right) B\dot{\varepsilon}_m\right] \quad (18)$$

For an experimental condition which results in a given strain rate, the time corresponding to the minimum creep rate can be approximatively provided by an equation in the form

$$\dot{\varepsilon}_m t_m = c_m \quad (19)$$

with c_m=5.94x10^{-3} (time in s). This estimation, obtained from the single test in Figure 4, proved to be substantially correct for all the curves obtained in the study presented.

The last parameter to be determined is the *B* constant. In this case, the particle size and distribution in the crept samples were not quantitatively analyzed, since this was well beyond the scope of the study. Thus, an estimate of the *B* value had to be obtained by fitting one of the experimental data, for example again the value of the minimum creep rate from Figure 4. An excellent result is obtained with *B*=10 s^{-1}. Once *B* is determined, the size of the particle, hence the interparticle distance *L*, in correspondence of a given minimum creep rate can be easily obtained, and then the corresponding stress in the MM can be calculated by Equations (2) - (7). The model curves are presented in Figure 9. No other fitting was carried out, except the aforementioned calculation of *B* from the 175°C – 200 MPa experiment. The agreement between the curves for the MM and the experimental data is excellent, with significant deviations being observed only at 205°C and at 225°C in the low-stress regime.

Although the model was aimed at describing creep response, in principle it could be tentatively used to extrapolate the room-temperature behavior of the alloy, in form of maximum stress for a given strain rate, that is, as stress to fracture obtained by tensile testing, to be compared with the maximum strength condition in creep, i.e. to the minimum creep rate at a given stress. In this case, no particle growth is expected. Thus the room-temperature model curve is also presented in Figure 9, which also shows the typical ranges of tensile strength reported in literature. An alloy with a

microstructure similar to the model here presented should exhibit a maximum tensile stress close to 400 MPa, which seems a quite reliable, if one conservative, estimate.

5.2 Creep of annealed alloy

The previous paragraph supports the accuracy of the model in describing the creep response of the alloy produced by AM. Yet, to be useful, the model should be able to predict the material behavior also in different initial states, for example after stress-relief annealing. If it is supposed that the MM described in section 2 undergoes annealing at 300°C for 2 h, as in the case of the alloy tested by Elan Uzan et al [14], then, according to Equation (14), after annealing, the initial population of 50 nm particles coarsens up to 128 nm. By taking d_0=128 nm, the model curves for the tests carried out at 225°C and at room temperature can be easily obtained. The model curves are presented in Figure 10 and compared with the experimental data at 225°C [14] and at room temperature [36]. No fitting at all was required, since the same model and the same parameters of the previous section were used. The agreement between experiments and curves is remarkably accurate, particularly if it is taken into account that the as-deposited microstructure of the alloy tested in [14] was somewhat different from that of the MM. In any case, the enlarged scale in the Figure does not gives justice of the relative accuracy of the model even at room temperature, since the difference between estimated and measured value of the maximum strength condition merely ranges between 5 and 7%.

5.3 Final remarks

The discussion above indicates that the model here presented could become a powerful tool to predict the material behavior, once a few preliminary data are available. Nevertheless, the comparison between the extremely simplified microstructure of the MM and the complex structure of the AlSi10Mg alloy deserves a few additional comments.

The first point to be analyzed is the difference between Figure 1a and the microstructure shown in Figure 3. Figure 11 overlaps an example of the microstructure of the real alloy and an inset from the

MM scheme of Figure 1. The Figure clearly shows that the almost continuous network of smaller Si-rich particles of Figure 3 is somewhat different from the dispersion of 50nm equiaxed particles in the eutectic regions in Figure 1. Yet, high-temperature exposure results in Si spheroidization [14]. Thus, the actual microstructure of the crept sample becomes even more similar to the one reported in Fig.1b. This observation implies that the model provides a better description of the actual microstructure than one can expect by merely comparing Figures 1a and 3.

The second important point is that the more accurate the prediction of the particle size, that is, of the coarsening/ripening phenomena, all the more accurate the model. Ostwald ripening is commonly used to describe Si particles evolution during annealing [37,38], this is the reason why the corresponding 3^{rd}-power equation was used in Section 2.3. Although the determination of the physically-correct coarsening law falls well beyond the limited scopes of the study presented (an overview of the complexity of these phenomena in multicomponent alloys can be found, for example, in [39]), a comparison with other literature data [40], which indeed refer to coarse Si annealed at much higher temperatures, seems to suggest that the equation proposed tends to overestimate particle size for long times of exposure. Yet, the available data are still too scarce to provide an accurate description of the complex coarsening phenomena of ultra-fine Si particles occurring during straining at low temperatures. In addition, the presence of as other phases, like Mg_2Si, was not considered. These problems will obviously affect the accuracy of any model attempting to predict the creep response of AlSi10Mg or similar alloys.

Another significant point is that, as mentioned above, the model does not take into account the heterogeneities of the mesostructure typical of AM-products (size of the columnar grains, effect of overlapping melt-pools etc.). On the other hand, the predictions of the model are sufficiently accurate to confirm that the main mechanisms governing the creep rate is the interaction between particles and dislocations, while the other microstructural issues could play a significant role only by influencing damage mechanisms, leading to early fracture and to the relatively large scatter of the data.

6. Conclusions

In the study presented, the creep response of the AlSi10Mg alloy was investigated. In particular, the ultra-fine microstructure typical of similar alloys produced by additive manufacturing was modelled by assuming that the material was constituted by a combination of soft (the cell interiors) and hard (the eutectic network) zones. The major source of strengthening was identified in the presence of ultra-fine Si particles. A physically-based set of constitutive equations which also took into account the Ostwald ripening phenomena and the accelerating effects of strain on the progressive softening of the alloy was then used to predict the creep response of the model material in terms of minimum creep rate dependence on applied stress. The model curves were then compared with experimental data obtained by testing the as-deposited alloy between 150 and 225°C. In addition, the effect of annealing was also considered by comparing the prediction of the model with the only other dataset available in literature. Notwithstanding the lack of a truly accurate description of the coarsening/ripening phenomena, the agreement between the model curves and the experimental data was more than encouraging. This fact confirmed that the proposed combination of a simplified material-model and a proper set of constitutive equations represents an excellent tool for predicting the response of the alloy.

7. Acknowledgements

This research was made possible by the Grant of Excellence Departments, MIUR-Italy (ARTICOLO 1, COMMI 314-337 LEGGE 232/2016).

Appendix1: Constitutive model derivation

The constitutive model, developed for Cu by Sandström [18–20] and discussed at length [21–24], is based on the well-known Taylor equation, here simplified in the form

$$\sigma = \sigma_0 + \sigma_p = \sigma_0 + \alpha m G b \sqrt{\rho} \qquad [A1]$$

where m is the Taylor factor (m = 3.06 for fcc metals), ρ is the dislocation density, G is the shear modulus, α=0.3, b is the length of the Burgers vector and $\sigma_\rho = \alpha m G b \rho^{1/2}$ is the dislocation hardening term. The stress σ_0 represents the strengthening contribution due to the interaction between fine particles and dislocations. Equation [A1] does not take into account the stress required to move the dislocation in the absence of other dislocations nor the viscous drag stress due to solute atoms, since both these quantities, in a dilute solid solution, are usually much lower than the strengthening term due to particle-dislocation interaction.

The evolution of dislocation density during straining can be expressed as [18–20]

$$\frac{d\rho}{d\varepsilon} = \frac{m}{bL^*} - \omega\rho - \frac{2}{\dot{\varepsilon}} M_{cg} \tau_l \rho^2 \qquad \text{[A2]}$$

where ω is a constant, τ_l is the dislocation line tension (τ_l=0.5Gb^2), M_{cg} is the dislocation mobility and L^* is the dislocation mean free path, i.e the distance travelled by a dislocation before it undergoes a reaction. The first term on the right-hand side of Eqn.[A2] represents the strain hardening effect due to dislocation multiplication, which is more rapid when L^* and C_L assume low values and/or the dislocation density is high. The second and third terms on the right-hand side of Eqn. [A2] describe the effect of recovery. Since at high temperature, the last term largely predominates on the second term, this was omitted. Thus the equation can be simplified to

$$\frac{d\rho}{d\varepsilon} = \frac{m}{bL^*} - \frac{2}{\dot{\varepsilon}} M_{cg} \tau_l \rho^2 \qquad \text{[A3]}$$

The obstacles that the mobile dislocations meet during slip determine the slip length. Thus, in presence of a densely spaced distribution of fine particles interacting with dislocations, the dislocation mean free path can be expressed in the form [23,24]

$$\frac{1}{L^*} = \frac{\sqrt{\rho}}{C_L} + \frac{1}{L} \qquad \text{[A4]}$$

For alloys with a distribution of a densely spaced particles, Eqn.[A4] becomes

$$\frac{1}{L^*} \approx \frac{1}{L} \qquad \text{[A5]}$$

At steady state, combination of Eqns. [A1], [A3] and [A4] gives

$$\dot{\varepsilon}_m = \frac{2M_{cg}\tau_l bL}{m}\left(\frac{\sigma_\rho}{\alpha mGb}\right)^4 \quad [A6]$$

Dislocation mobility in pure Al can be expressed as

$$M_{cg} \cong \frac{D_{0L}b}{kT} exp\left(\frac{\sigma_\rho b^3}{kT}\right) exp\left\{-\frac{Q_L}{RT}\left[1-\left(\frac{\sigma_\rho}{R_{max}}\right)^2\right]\right\} \quad [A7]$$

while in dilute Al-X solid solutions (where X is either Si or Mg, in this case) it becomes [18–20]

$$M_{cg} \cong \frac{D_{0L}b}{kT} exp\left(\frac{\sigma_\rho b^3}{kT}\right) exp\left\{-\frac{Q_L}{RT}\left[1-\left(\frac{\sigma_\rho}{R_{max}}\right)^2\right]\right\} exp\left(-\frac{U_{ss}}{RT}\right) \quad [A8]$$

where R_{max} is the maximum strength of the alloy, tentatively quantified at room temperature as 1.5 times the ultimate tensile strength (R_{UTS}) of the alloy. The U_{ss} term, which describes the energy necessary for solute atoms to jump in and out of the solute clouds formed around dislocations, assumes the form [19]

$$U_{ss} = \frac{1}{3\pi}\ \frac{1+\nu}{1-\nu}\ \frac{G\Omega\delta R}{k} \quad [A9]$$

where ν is the Poisson's ratio (=0.3 in Al), Ω is the average Al-atomic volume and δ is the volume atomic misfit.

References

[1] N.T. Aboulkhair, M. Simonelli, L. Parry, I. Ashcroft, C. Tuck, R. Hague, 3D printing of Aluminium alloys: Additive Manufacturing of Aluminium alloys using selective laser melting, Prog. Mater. Sci. (2019). https://doi.org/10.1016/j.pmatsci.2019.100578.

[2] D. Herzog, V. Seyda, E. Wycisk, C. Emmelmann, Additive manufacturing of metals, Acta Mater. (2016). https://doi.org/10.1016/j.actamat.2016.07.019.

[3] T. DebRoy, H.L. Wei, J.S. Zuback, T. Mukherjee, J.W. Elmer, J.O. Milewski, A.M. Beese, A. Wilson-Heid, A. De, W. Zhang, Additive manufacturing of metallic components –

Process, structure and properties, Prog. Mater. Sci. (2018). https://doi.org/10.1016/j.pmatsci.2017.10.001.

[4] U. Scipioni Bertoli, G. Guss, S. Wu, M.J. Matthews, J.M. Schoenung, In-situ characterization of laser-powder interaction and cooling rates through high-speed imaging of powder bed fusion additive manufacturing, Mater. Des. (2017). https://doi.org/10.1016/j.matdes.2017.09.044.

[5] R.J. Hebert, Viewpoint: metallurgical aspects of powder bed metal additive manufacturing, J. Mater. Sci. (2016). https://doi.org/10.1007/s10853-015-9479-x.

[6] J. Wu, X.Q. Wang, W. Wang, M.M. Attallah, M.H. Loretto, Microstructure and strength of selectively laser melted AlSi10Mg, Acta Mater. (2016). https://doi.org/10.1016/j.actamat.2016.07.012.

[7] M. Fousová, D. Dvorský, A. Michalcová, D. Vojtěch, Changes in the microstructure and mechanical properties of additively manufactured AlSi10Mg alloy after exposure to elevated temperatures, Mater. Charact. (2018). https://doi.org/10.1016/j.matchar.2018.01.028.

[8] A. Iturrioz, E. Gil, M.M. Petite, F. Garciandia, A.M. Mancisidor, M. San Sebastian, Selective laser melting of AlSi10Mg alloy: influence of heat treatment condition on mechanical properties and microstructure, Weld. World. (2018). https://doi.org/10.1007/s40194-018-0592-8.

[9] N.E. Uzan, R. Shneck, O. Yeheskel, N. Frage, Fatigue of AlSi10Mg specimens fabricated by additive manufacturing selective laser melting (AM-SLM), Mater. Sci. Eng. A. (2017). https://doi.org/10.1016/j.msea.2017.08.027.

[10] N. Takata, H. Kodaira, A. Suzuki, M. Kobashi, Size dependence of microstructure of AlSi10Mg alloy fabricated by selective laser melting, Mater. Charact. (2018). https://doi.org/10.1016/j.matchar.2017.11.052.

[11] N. Read, W. Wang, K. Essa, M.M. Attallah, Selective laser melting of AlSi10Mg alloy: Process optimisation and mechanical properties development, Mater. Des. (2015).

https://doi.org/10.1016/j.matdes.2014.09.044.

[12] I. Rosenthal, R. Shneck, A. Stern, Heat treatment effect on the mechanical properties and fracture mechanism in AlSi10Mg fabricated by additive manufacturing selective laser melting process, Mater. Sci. Eng. A. 729 (2018) 310–322. https://doi.org/10.1016/j.msea.2018.05.074.

[13] K.G. Prashanth, S. Scudino, H.J. Klauss, K.B. Surreddi, L. Löber, Z. Wang, A.K. Chaubey, U. Kühn, J. Eckert, Microstructure and mechanical properties of Al-12Si produced by selective laser melting: Effect of heat treatment, Mater. Sci. Eng. A. (2014). https://doi.org/10.1016/j.msea.2013.10.023.

[14] N.E. Uzan, R. Shneck, O. Yeheskel, N. Frage, High-temperature mechanical properties of AlSi10Mg specimens fabricated by additive manufacturing using selective laser melting technologies (AM-SLM), Addit. Manuf. (2018). https://doi.org/10.1016/j.addma.2018.09.033.

[15] S. Spigarelli, M. Cabibbo, E. Evangelista, S. Cucchieri, Evaluation of the creep properties of an Al-17Si-1Mg-0.7Cu alloy, Mater. Lett. (2002). https://doi.org/10.1016/S0167-577X(02)00677-8.

[16] S. Spigarelli, E. Evangelista, S. Cucchieri, Analysis of the creep response of an Al-17Si-4Cu-0.55Mg alloy, Mater. Sci. Eng. A. (2004). https://doi.org/10.1016/j.msea.2004.06.043.

[17] S. Spigarelli, Constitutive equations in creep of Mg-Al alloys, Mater. Sci. Eng. A. (2008). https://doi.org/10.1016/j.msea.2008.03.007.

[18] R. Sandström, Basic model for primary and secondary creep in copper, Acta Mater. 60 (2012) 314–322. https://doi.org/10.1016/j.actamat.2011.09.052.

[19] R. Sandström, Influence of phosphorus on the tensile stress strain curves in copper, J. Nucl. Mater. 470 (2016) 290–296. https://doi.org/10.1016/j.jnucmat.2015.12.024.

[20] R. Sandström, The role of cell structure during creep of cold worked copper, Mater. Sci. Eng. A. 674 (2016) 318–327. https://doi.org/10.1016/j.msea.2016.08.004.

[21] S. Spigarelli, R. Sandström, Basic creep modelling of Aluminium, Mater. Sci. Eng. A. 711 (2018) 343–349. https://doi.org/10.1016/j.msea.2017.11.053.

[22] S. Spigarelli, C. Paoletti, A unified physical model for creep and hot working of Al-Mg solid solution alloys, Metals (Basel). 8 (2018) 1–14. https://doi.org/10.3390/met8010009.

[23] S. Spigarelli, C. Paoletti, A new model for the description of creep behaviour of aluminium-based composites reinforced with nanosized particles, Compos. Part A Appl. Sci. Manuf. 112 (2018). https://doi.org/10.1016/j.compositesa.2018.06.021.

[24] C. Paoletti, M. Regev, S. Spigarelli, Modelling of creep in alloys strengthened by rod-shaped particles: Al-Cu-Mg age-hardenable alloys, Metals (Basel). 8 (2018) 1–18. https://doi.org/10.3390/met8110930.

[25] E. Orowan, Dislocations in metals, ed. Cohen, M. The Institute of Metals Division, the American Institute of Mining and metallurgical engineers, New York (NY), 1954.

[26] P. Yavari, F.A. Mohamed, T.G. Langdon, Creep and substructure formation in an Al-5% Mg solid solution alloy, Acta Metall. 29 (1981) 1495–1507. https://doi.org/https://doi.org/10.1016/0001-6160(81)90184-X.

[27] M. Taneike, M. Kondo, T. Morimoto, Accelerated Coarsening of MX Carbonitrides in 12%Cr Steels during Creep Deformation, ISIJ Int. (2001). https://doi.org/10.2355/isijinternational.41.Suppl_S111.

[28] S. Mrowec, Defects and Diffusion in Solids, Elsevier. (1980) Amsterdam.

[29] M. Legros, B. Kaouache, P. Gergaud, O. Thomas, G. Dehm, T.J. Balk, E. Arzt, Pipe-diffusion ripening of Si precipitates in Al-0.5%Cu-1%Si thin films, Philos. Mag. (2005). https://doi.org/10.1080/14786430500228374.

[30] T. Nakajima, M. Takeda, T. Endo, Accelerated coarsening of precipitates in crept Al-Cu alloys, Mater. Sci. Eng. A. (2004). https://doi.org/10.1016/j.msea.2004.01.131.

[31] F.S. Buffington, M. Cohen, Self-Diffusion in Alpha Iron Under Uniaxial Compressive Stress, JOM. (1952). https://doi.org/10.1007/bf03398152.

[32] S. Spigarelli, Microstructure-based assessment of creep rupture strength in 9Cr steels, Int. J. Press. Vessel. Pip. (2013). https://doi.org/10.1016/j.ijpvp.2012.10.005.

[33] S. Spigarelli, Quantification of the effect of early microstructural degradation during creep of 9Cr-1Mo-NbV steels at 600°C, Mater. Sci. Eng. A. (2013). https://doi.org/10.1016/j.msea.2012.12.056.

[34] T. Nakajima, S. Spigarelli, E. Evangelista, T. Endo, Strain Enhanced Growth of Precipitates during Creep of T91, Mater. Trans. (2003). https://doi.org/10.2320/matertrans.44.1802.

[35] T. Nakajima, M. Takeda, T. Endo, Strain enhanced precipitate coarsening during creep of a commercial magnesium alloy AZ80, Mater. Trans. (2006). https://doi.org/10.2320/matertrans.47.1098.

[36] I. Rosenthal, A. Stern, N. Frage, Strain rate sensitivity and fracture mechanism of AlSi10Mg parts produced by Selective Laser Melting, Mater. Sci. Eng. A. (2017). https://doi.org/10.1016/j.msea.2016.11.070.

[37] S. Fujikawa, Y. Oyobiki, K.I. Hirano, Studies on Solid Solubility of Silicon in Aluminum and Ostwald Ripening of Si Precipitates in Al-Si alloys by means of Electrical Resistivity Measurement, J. Japan Inst. Light Met. (1979). https://doi.org/10.2464/jilm.29.331.

[38] R.M. Gomes, T. Sato, A. Kamio, Microstructures and coarsening behavior of silicon particles in P/M Al-Si-Cu-Mg alloys containing Fe and Ni, Keikinzoku/Journal Japan Inst. Light Met. (1997). https://doi.org/10.2464/jilm.47.90.

[39] K. Kim, P.W. Voorhees, Ostwald ripening of spheroidal particles in multicomponent alloys, Acta Mater. (2018). https://doi.org/10.1016/j.actamat.2018.04.041.

[40] F.N. Rhines, M. Aballe, GROWTH OF SILICON PARTICLES IN AN ALUMINUM MATRIX., Metall. Trans. A, Phys. Metall. Mater. Sci. (1986). https://doi.org/10.1007/BF02645912.

List of Figure captions

Figure 1. a) Schematic representation of the MM microstructure formed by Al cells surrounded by a network of discrete Si particles; b) the same structure at the same magnification after few particles underwent Ostwald ripening, which doubled their diameter, while the a higher number dissolved. Although still in their original location, the surviving particles appear to have a far more homogeneous distribution.

Figure 2. Calculation of the increase in particle size by Ostwald ripening for Si (data from [13]).

Figure 3. Representative micrograph of the typical microstructure at sub-micron scale. Although the general morphology remains similar, the cell size somewhat changes in different locations of the sample (compare a. and b., the latter being in the heat-affected zone).

Figure 4. A magnified region from which EDS point analyses were performed at dark-grey rounded particles (red spot in the Figure) and at the Al-matrix (blue spot in the Figure).

Figure 5. Representative example (175°C-200 MPa) of the shape of the creep curves.

Figure 6. Tipycal shape of the creep curves: a. strain rate vs time; b. strain rate vs strain.

Figure 7. Minimum creep rate dependence on applied stress.

Figure 8. Hardness variation with time of exposure at 150 and 205°C, measured on the samples' heads and the gauge length after testing under different loads. The test duration does not include heating and soaking time at testing temperature (roughly 3h in total). The figure also plots the hardness of the as-deposited samples (145±7 HV).

Figure 9. Model curves for the minimum creep rate dependence on applied stress for MM compared with experimental data. The Figure also plots the model curve describing the maximum strength for a given strain rate and the range of experimental stress to fracture observed in literature (broken line) [6,7,9,11,12].

Figure 10. Minimum creep rate at 225°C [14] and tensile strength under different strain rates at room temperature [36] for an alloy stress relieved at 300°C for 2h. The Figure plots also the curves calculated by the constitutive model here discussed.

Figure 11. Qualitative comparison between the microstructure of the as-deposited alloy (Figure 3) and the schematic drawing of the MM structure of Figure 1 (inset).

Table 1. List of constitutive model parameters (see [21–24] for a detailed description).

symbol	meaning
σ	applied stress [MPa]
$\dot{\varepsilon}_m$	minimum creep rate [s^{-1}]
σ_0	particle strengthening term [MPa]
α	constant: 0.3
m	Taylor factor: 3.06
R	gas constant: 8.314 [J $mol^{-1}K^{-1}$]
G	shear modulus: 30220-16 T [MPa] [26]
b	Burgers vector: $2.47x10^{-10}$ [m] [26]
ρ	dislocation density [m^{-2}]
σ_ρ	$\alpha mGb\rho^{1/2}$ dislocation hardening term: $=\alpha mGb\rho^{1/2}$ [MPa]
τ	dislocation line tension: $=0.5Gb^2$ [N]
R_{max}	maximum strength at the testing temperature [MPa]
k	Boltzmann constant $=1.38x10^{-23}$ [J K^{-1}]
D_{0L}	pre-exponential factor in the Arrhenius equation describing the temperature dependence of the vacancy diffusion coefficient: $8.3x10^{-6}$ [m^2s^{-1}] [21]
Q_L	activation energy in the Arrhenius equation describing the temperature dependence of the vacancy diffusion coefficient: 122 [kJ mol^{-1}] [21]
U_{ss}	energy necessary for Si (and Mg) atoms still in solid solution to jump in and out of the atmospheres that spontaneously form around dislocations; previous calculations gave for Mg values close to 10-15 kJ mol^{-1} [22,23] . For the sake of simplicity, here U_{ss} is assumed to be 10 [kJ mol^{-1}]
R^a_{UTS}	room temperature tensile strength of an alloy with the same impurity level, similar content of elements in solid solution and coarse intergranular intermetallics, in absence of fine Si particles, here roughly estimated to be 115 [MPa]
L	surface to surface interparticle spacing [m]
G_T G_{RT}	shear modulus at the testing temperature and at 25°C respectively [MPa]
M_{cg}	dislocation mobility

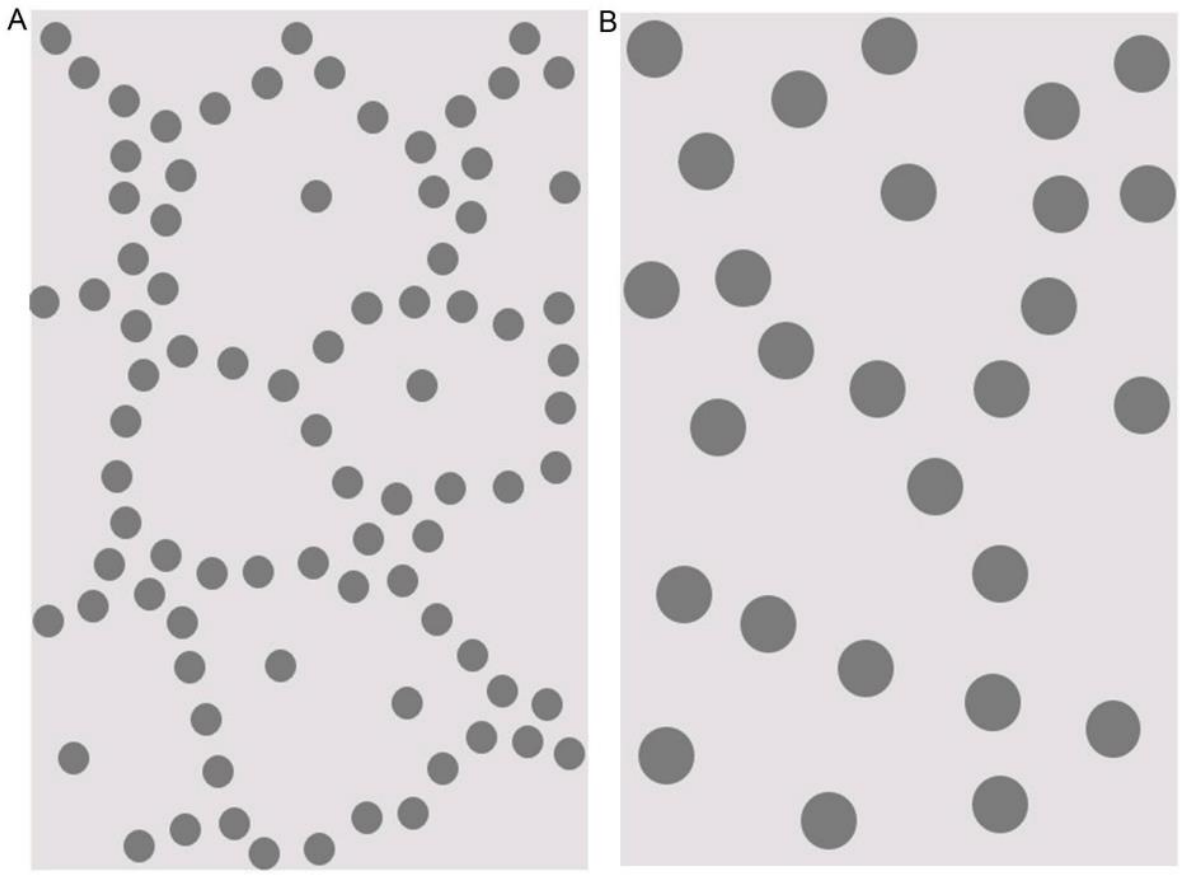

FIGURE 1

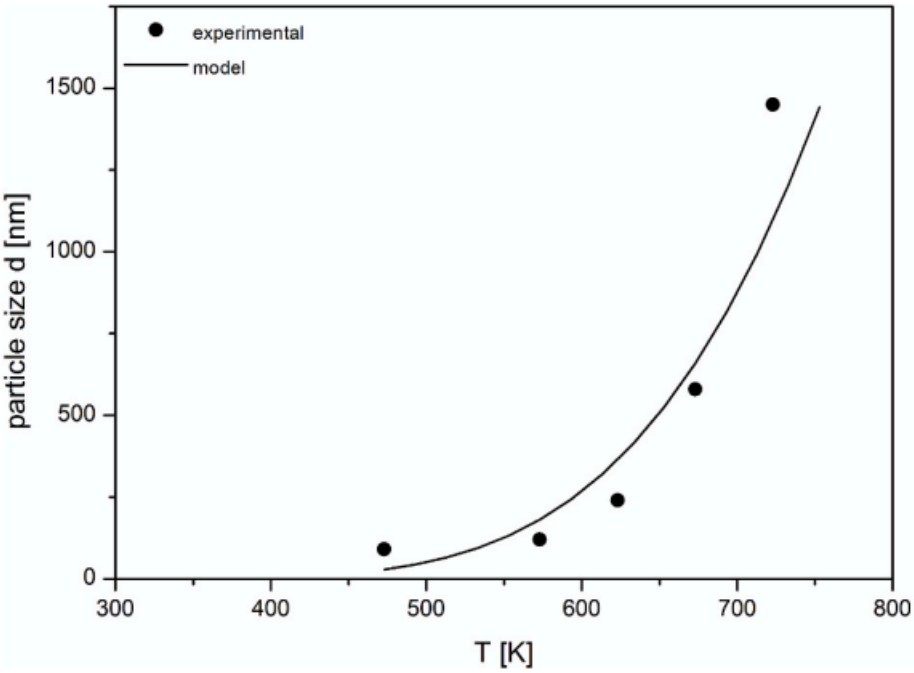

FIGURE 2

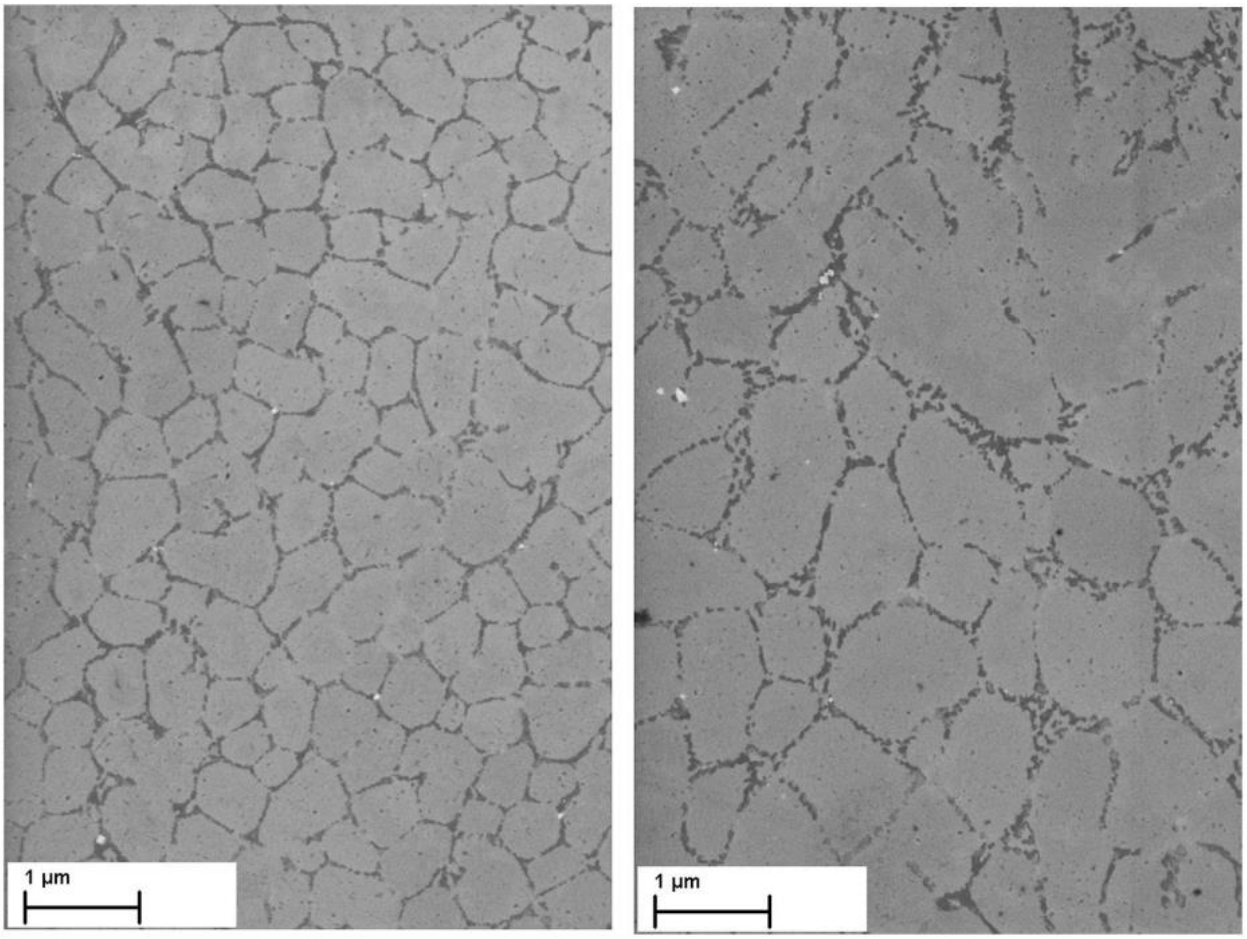

FIGURE 3

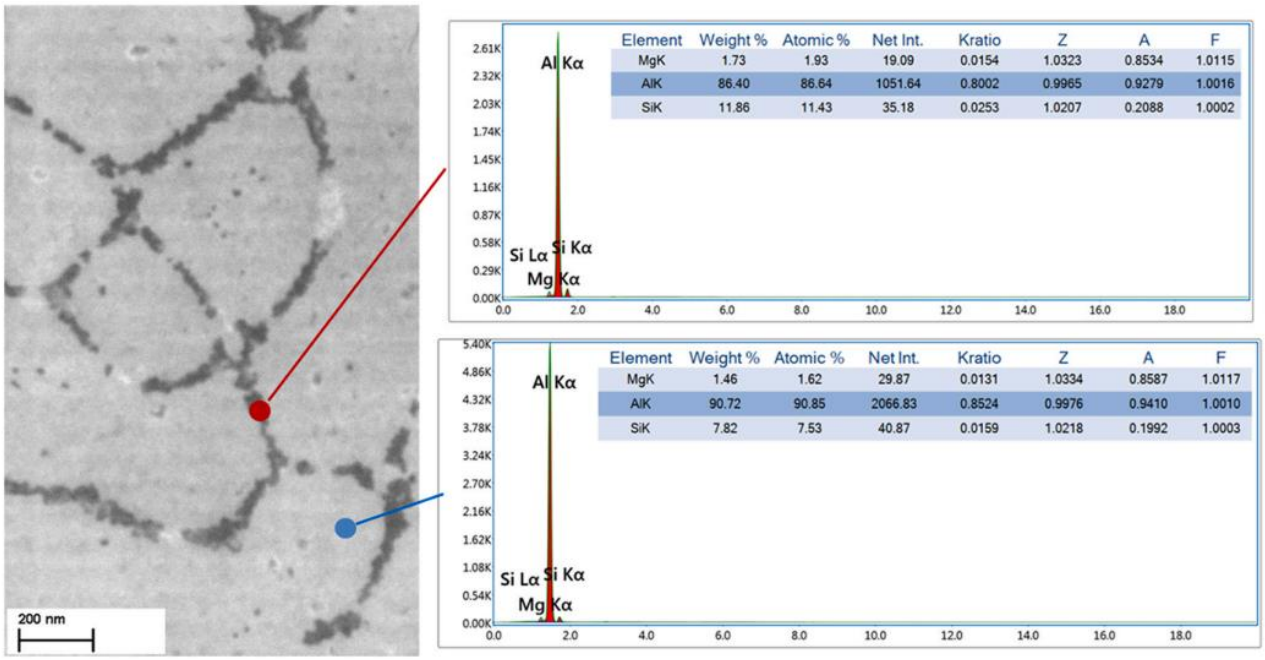

FIGURE 4

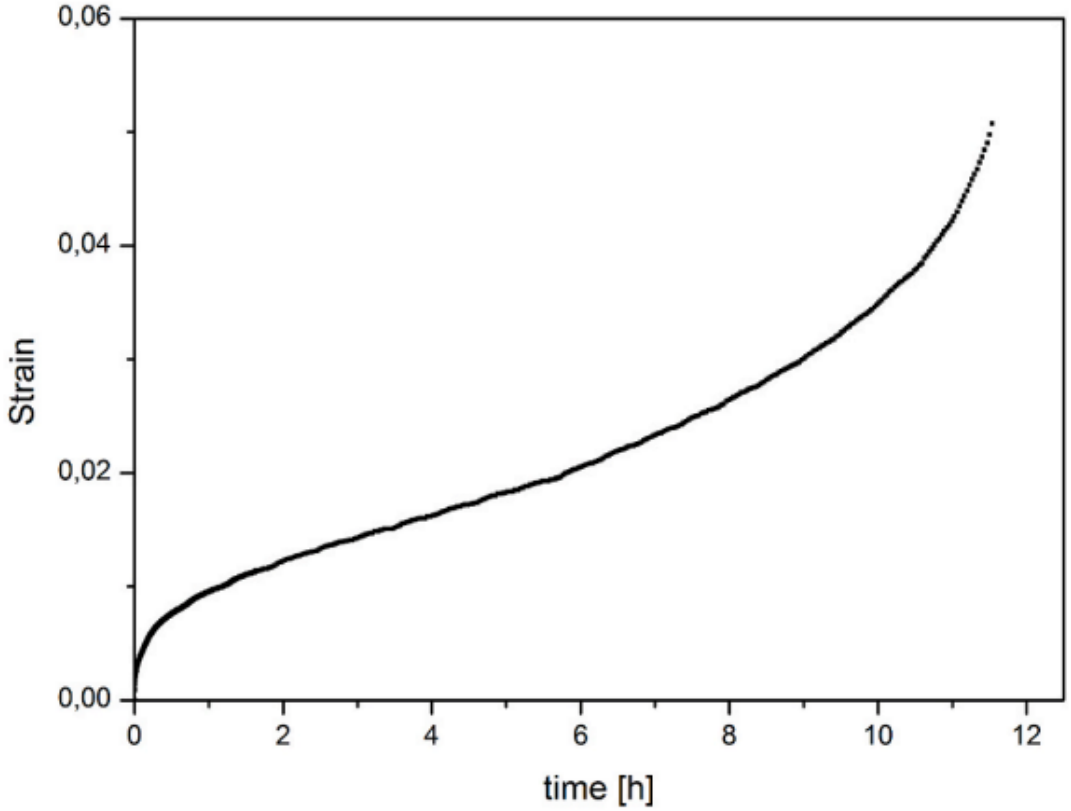

FIGURE 5

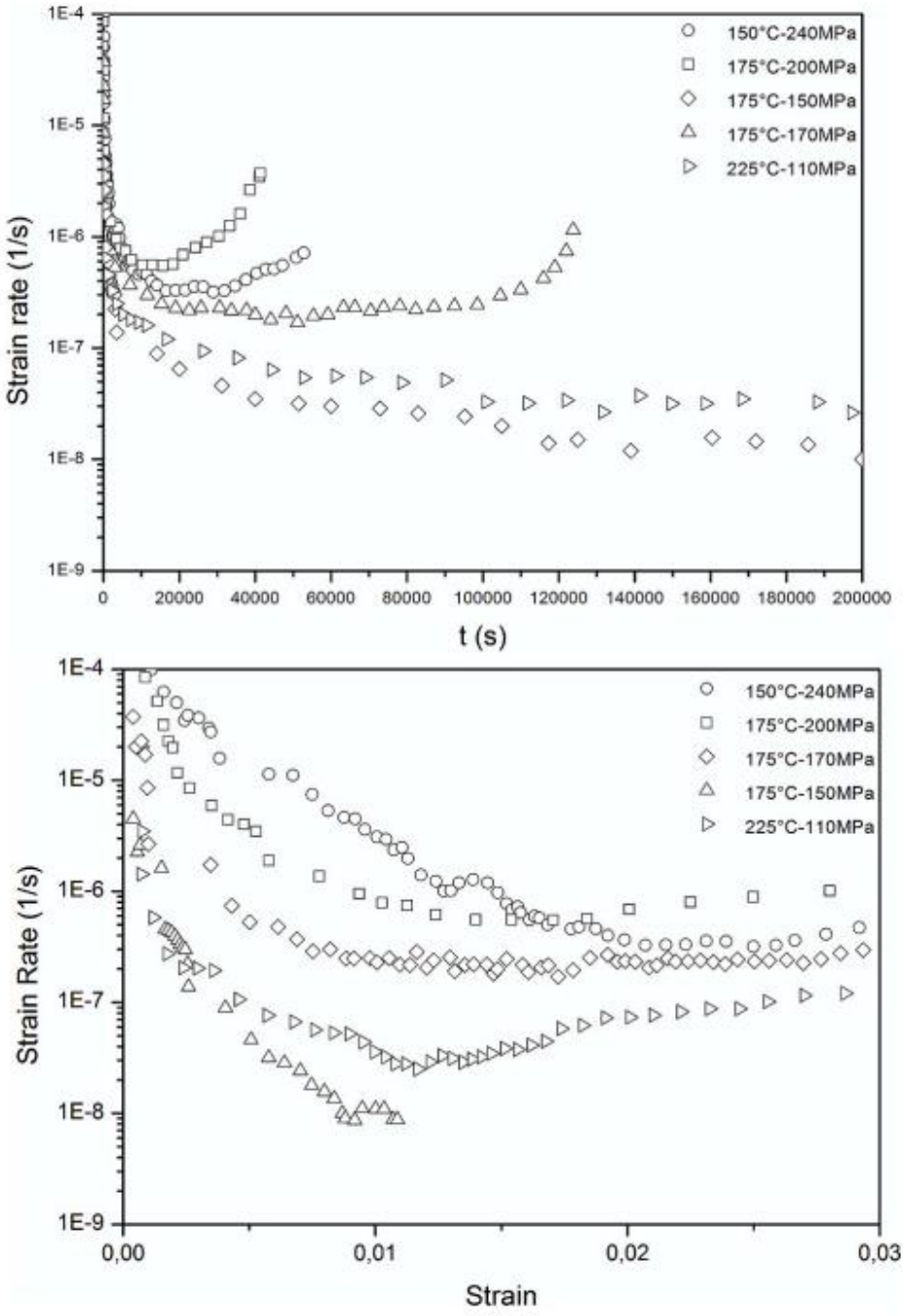
Strain rate (1/s)
1E-4
1E-5
1E-6
1E-7
1E-8
1E-9
0
20000
40000
60000
80000
100000
120000
140000
160000
180000
200000
t (s)
150°C-240MPa
175°C-200MPa
175°C-150MPa
175°C-170MPa
225°C-110MPa
Strain Rate (1/s)
1E-4
1E-5
1E-6
1E-7
1E-8
1E-9
0,00
0,01
0,02
0,03
Strain
150°C-240MPa
175°C-200MPa
175°C-170MPa
175°C-150MPa
225°C-110MPa

FIGURE 6

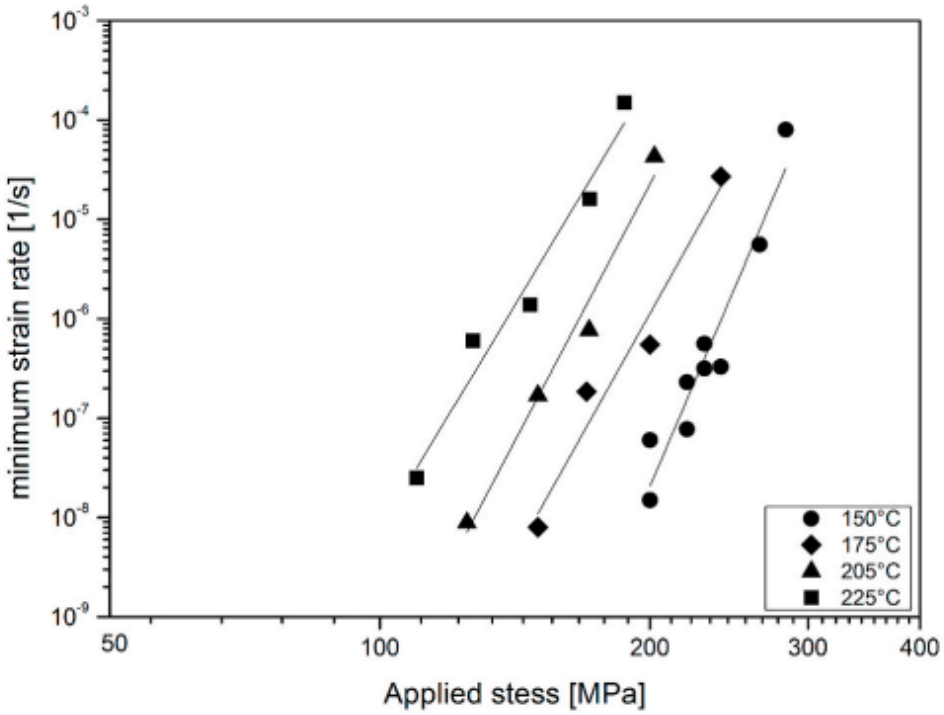

FIGURE 7

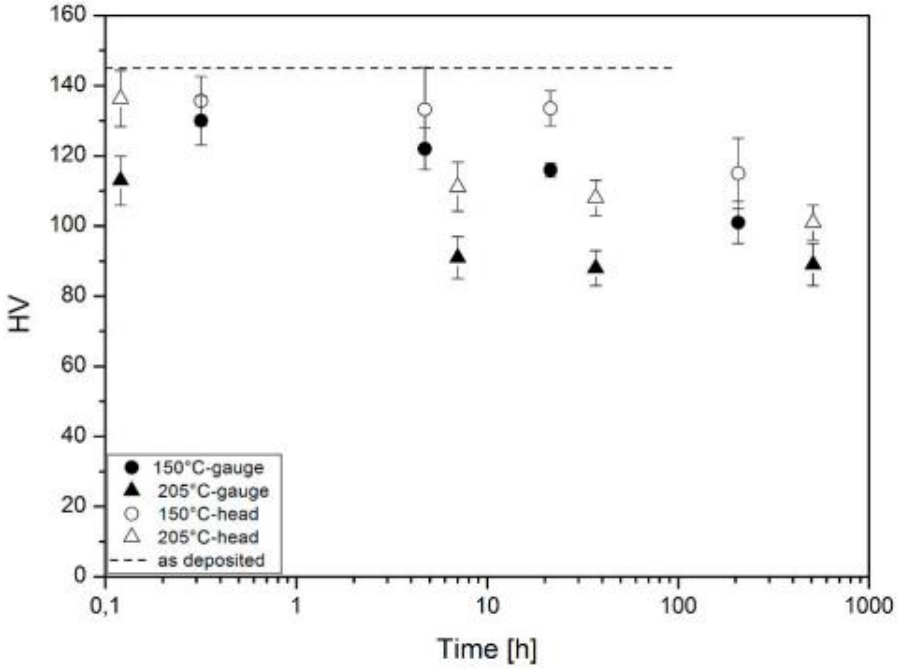

FIGURE 8

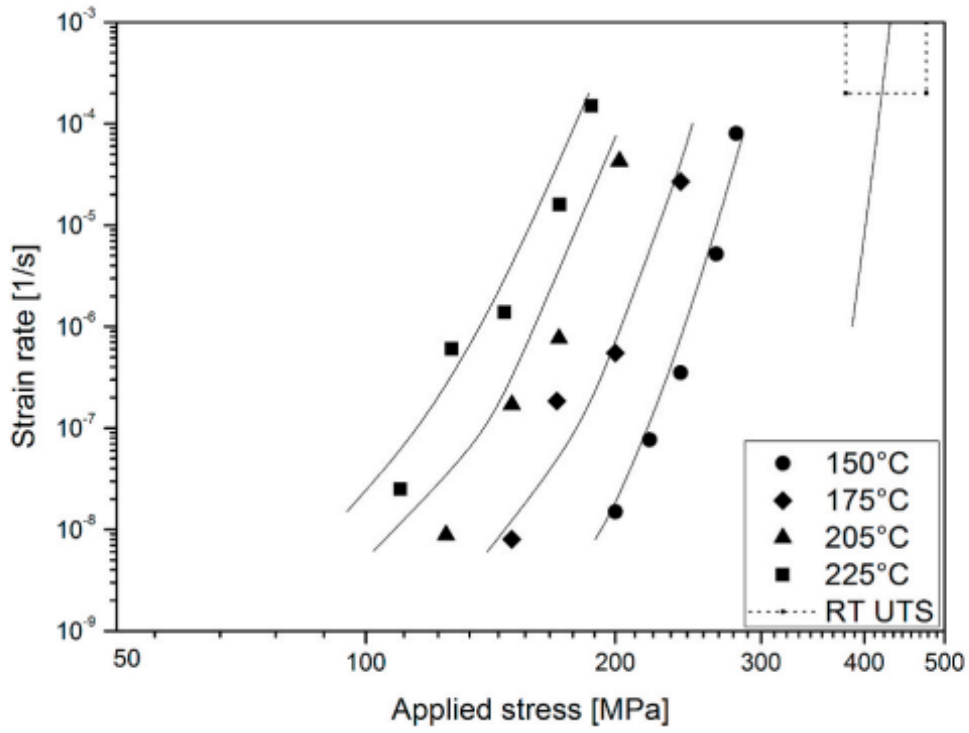

FIGURE 9

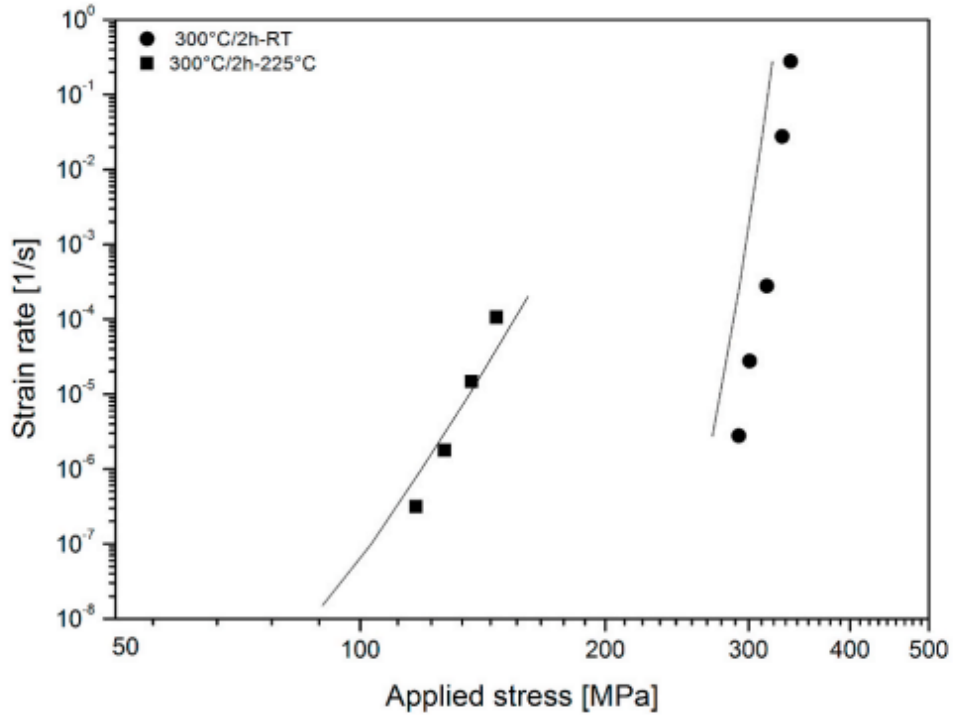

FIGURE 10

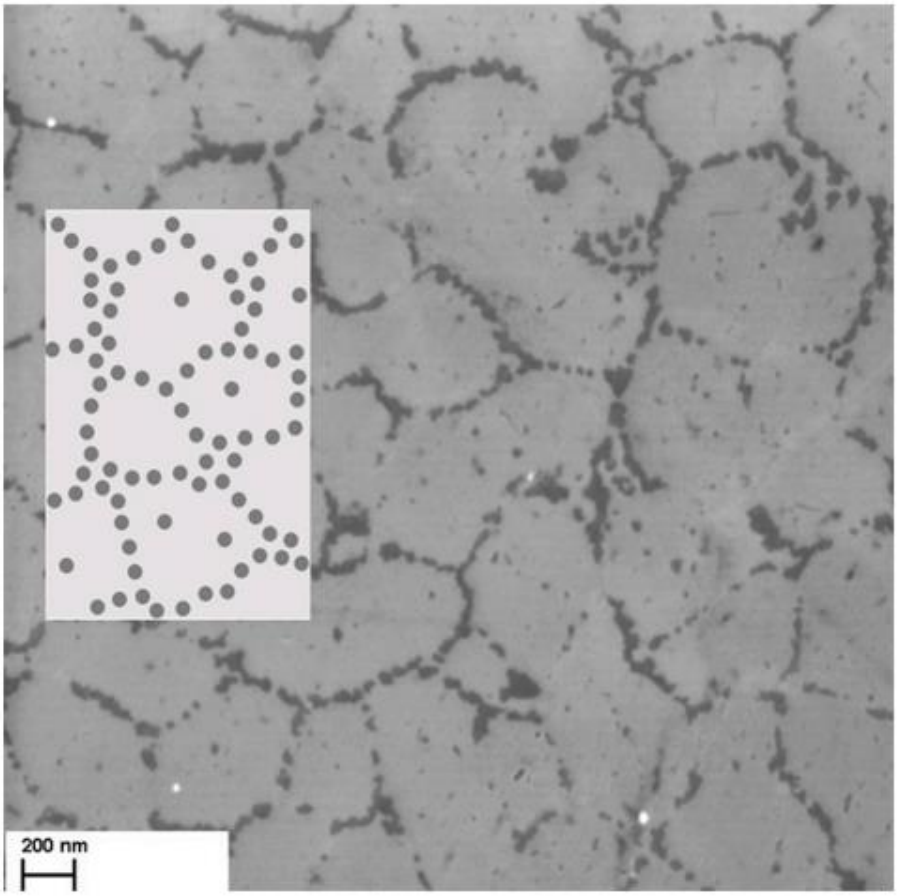

FIGURE 11